Estimation of seismic attenuation of the Greenland Ice Sheet using 3-D waveform modeling

Genti Toyokuni[1*], Masanao Komatsu[2], and Hiroshi Takenaka[2]

[1] Department of Geophysics, Graduate School of Science, Tohoku University, Sendai 980-8578, Japan

[2] Department of Earth Sciences, Okayama University, 3-1-1 Tsushima-naka, Kita-ku, Okayama 700-8530, Japan

Submitted to ***Journal of Geophysical Research: Solid Earth*** in December 2020

*Corresponding author:

Genti Toyokuni

E-mail: toyokuni@tohoku.ac.jp

ORCID ID: 0000-0003-3786-207X

Key Points:

- Seismic attenuation of the Greenland Ice Sheet is estimated by comparing the observed and theoretical Rayleigh waveforms.
- The quality (Q) factor of the ice sheet is approximately 10−50 for both *P* and *S* waves, indicating extremely high attenuation.
- This is the first Q estimation targeting the ice sheet using waves with a propagation distance of more than 100 km.

Abstract

We estimated the seismic attenuation (Q factor) of the Greenland Ice Sheet (GrIS) by comparing observed and theoretical Rayleigh waveforms. Observed waveforms are obtained by interfering with noise waveforms in vertical-component seismograms between stations, which belong to the latest broadband seismic network distributed throughout Greenland (GLISN network). Theoretical waveforms are calculated by parallel computation with the latest 3-D seismic waveform modeling. Comparing the observed waveforms with the theoretical waveforms at different Q factors reveals that GrIS has a low Q of Q_P, $Q_S \leq 50$, indicating very high attenuation of seismic waves due to the ice. This study is the first to confirm the low Q factor of ice sheets via ultra-long-distance propagation (~several hundreds to 1,000 km). The Q factors obtained in this study are indispensable for estimating the thermal status of GrIS, as well as for interpreting the characteristics of seismic waveform that propagates through GrIS.

Key words:

Q factor, Greenland Ice Sheet (GrIS), 3-D modeling, finite-difference method (FDM), seismic attenuation, The Greenland Ice Sheet Monitoring Network (GLISN)

1. Introduction

The Greenland Ice Sheet (GrIS) occupies 80% of the total area of Greenland, with an average thickness of ~2 km and a maximum thickness of > 3 km (Bamber, Ekholm, et al., 2001; Bamber, Layberry, et al., 2001; Henriksen et al., 2009). If the GrIS melts completely, the global sea levels will rise by 7 m (Houghton et al., 2001); therefore, an accurate prediction of its thermal state is desirable. Until recently, there were only a few permanent seismic stations in and around Greenland; however, since the launch of the Greenland Ice Sheet Monitoring Network (GLISN) in 2009, the number has gradually increased, with 34 currently operating stations, including four on the GrIS (Clinton et al., 2014; Toyokuni et al., 2014). The GLISN is an international network involving 11 countries (Canada, Denmark, France, Germany, Italy, Japan, Norway, Poland, South Korea, Switzerland, and the United States). The data on three-component broadband seismic waveforms obtained by GLISN have been made public worldwide through the Data Management Center (DMC), which is a branch of the U.S. Incorporated Research Institutions for Seismology (IRIS). Numerous seismological studies have used GLISN data (e.g., Darbyshire et al., 2018; Lebedev et al., 2017; Levshin et al., 2017; Mordret, 2018; Mordret et al., 2016; Pourpoint et al., 2018; Rickers et al., 2013; Toyokuni et al., 2018, 2020a, 2020b); however, there is only one theoretical study on seismic waveform propagation through the GrIS (Toyokuni et al., 2015), which only used the elastodynamic equation, not accounting for anelastic attenuation.

Seismic attenuation, which is one of the basic physical properties of solids, is quantified by the quality (Q) factor. The Q factor of ice strongly depends on the thermal state, fabrics, observation area and depth, and frequency band (e.g., Peters et al., 2012; Podolskiy & Walter, 2016). Most Q factors of ice obtained in previous studies were for ice columns and were

obtained using measurements of the basal or deep englacial reflected waves (e.g., Westphal, 1965; Clee et al., 1969; Langleben, 1969; Gusmeroli et al., 2010; Peters et al., 2012). However, these Q factors vary widely from 7 to 1,000, owing to the dependency on the factors mentioned above. To accurately grasp the thermal state inside the GrIS and understand the characteristics of seismic waveforms observed by the GLISN network, we must know the Q factor averaged over the GrIS for *P* (Q_P) and *S* waves (Q_S) during long-distance propagation.

Helmstetter et al. (2015) fitted *P*- and *S*-waveforms of icequakes observed at Glacier d'Argentière in Mont Blanc, France, with synthetic waveforms, and estimated the Q factor of the glacier as Q_P, Q_S = 20. The horizontal propagation distances of seismic waves in their observations were up to ~200 m, and the glacier thickness was ~150−200 m. The frequency band of the waveforms was 30–500 Hz. To date, there are no other examples of Q factor estimations for glaciers or ice sheets by comparing the observed and theoretical waveforms. The purpose of this study is to obtain the average Q_P and Q_S of the GrIS by fitting the observed and theoretical surface waveforms that propagate through the GrIS over long distances (~100−1,000 km). The observed waveforms are ambient-noise Rayleigh waveforms extracted by seismic interferometry (Toyokuni et al., 2018) in a frequency band of 0.1−0.3 Hz. The theoretical waveforms are calculated with various Q_P and Q_S of the GrIS, using the latest full 3-D seismic waveform modeling scheme, that is, the quasi-Cartesian finite-difference method (FDM) (Takenaka et al., 2017).

2. Method

2.1 Extraction of observed Green's function

The cross-correlation waveforms for 120 GLISN station pairs were obtained by seismic interferometry (Toyokuni et al., 2018). The data period amounted to 4.5 years, ranging from September 1, 2011, to February 29, 2016. They used the vertical component of the noise waveforms (20 sps) at 16 GLISN stations (Figure 1a) and obtained the day-averaged cross-correlation functions (CCFs). The final CCF for each pair was obtained by averaging the daily waveforms over the entire analysis period (4.5 years). The CCF for a station pair can be converted to the Green's function when assuming one station as a source and the other as a receiver as follows:

$$\frac{d}{dt}\langle C_{12}(t)\rangle = c[G(t) - G(-t)] \quad (1)$$

where t is time, c is a constant, $\langle C_{12}(t)\rangle$ is the ensemble average of the CCF between stations 1 and 2, and $G(t)$ is Green's function (e.g., Roux et al., 2005; Nakahara, 2006). We use the 4.5-year averaged CCF as $\langle C_{12}(t)\rangle$. As the noise sources are unevenly distributed around GLISN stations, most of the CCFs have an asymmetrical shape with respect to the lag time. Therefore, after taking the time derivative of the 4.5-year averaged CCF according to Equation 1, the observed Green's function is obtained by folding back the negative lag time and averaging the causal and acausal portions. The time duration of the resulting Green's function is 600 s.

To extract clear Rayleigh wave packets, we select station pairs using the following procedure:

1. Apply a bandpass filter of the frequency band corresponding to the secondary microseisms (0.1−0.2 Hz or 0.1−0.3 Hz) that provides the highest energy.

2. Discard pairs whose maximum envelope amplitude does not fall within the typical Rayleigh-wave group-velocity range (2.7 km/s ≤ U ≤ 3.3 km/s). Through this process, pairs with an inter-station distance > 1,600 km are discarded because the Rayleigh wave packets for these pairs do not fall within the 600 s duration.

3. Divide the maximum envelope amplitude by the noise amplitude to calculate the signal-to-noise ratio (SNR). The noise amplitude is obtained by averaging the envelope amplitudes between 50 s before the theoretical arrival time, with U = 3.5 km/s, and 50 s after the theoretical arrival time, with U = 2.5 km/s. Pairs with SNR < 5 in the 0.1−0.2 Hz band are discarded (Figure 1b).

2.2 Calculation of synthetic Green's function

The theoretical Green's functions are calculated using the quasi-Cartesian finite-difference method (FDM) in Takenaka et al. (2017). In this method, the target region is transformed into coordinates near the equator, and the 3-D viscoelastodynamic equations are solved by the FDM in the local spherical coordinates. This method calculates seismic wave propagation on a grid distribution with nearly equal intervals in both the latitude and longitude directions, such as in the Cartesian coordinate system (= quasi-Cartesian coordinates) while preserving the curvature of the Earth. Therefore, this method is suitable for Greenland as it is an area of sub-global scale, and longitudinal intervals in the geometrical coordinates largely depend on the latitude. The coordinate transformation proposed by Takenaka et al. (2017) was also applied to Greenland and surrounding regions for the seismic tomography (Toyokuni et al.,

125 2020a,b). In addition, the quasi-Cartesian FDM can treat a point source with an arbitrary
126 mechanism (single force and moment-tensor source), 3-D structures of the density, seismic
127 velocities, and seismic attenuation, 3-D surface topography and structural discontinuities, and a
128 seawater layer.

129 As a substantial computational cost is required to manage the entirety of Greenland in the
130 3-D waveform modeling, we conduct computations for three smaller regions. Regions 1, 2, and 3
131 target the central, southern, and central-eastern parts of Greenland, respectively (Figure 1a). In
132 the coordinate transformation by Takenaka et al. (2017), the reference point near the center of
133 the target area is transformed into (longitude, latitude) = (90°, 0°). Table 1 lists the position of
134 the reference point and the calculation specifications for each region.

135 To obtain the vertical component of Green's function for a station pair, we impose a
136 vertically-oriented single force at the position of one station and calculate the vertical component
137 of the 3-D seismic waveforms at the position of another station. The source time function is a
138 bell-shaped pulse with a width of 1 s. To examine the differences in the results depending on the
139 grid used, Region 3 contains the station pairs used in Regions 1 and 2 (ICESG−SOEG and
140 ANGG−ICESG pairs, Figure 1a); however, the waveforms are calculated using a smaller spatial
141 grid interval and time increment than those in other regions.

142 We create structural models using the ETOPO1 Global Relief Model
143 (doi:10.7289/V5C8276M) for Greenland's surface topography, basal topography of the GrIS
144 (therefore, also for the thickness of the GrIS), and ocean bathymetry (Figures 2 and S1), and
145 using Crust 1.0 (Laske et al., 2013) for the 3-D density, *P*-wave velocity (V_P), and *S*-wave
146 velocity (V_S) in the GrIS, crust, and mantle. We note that, in our model, sedimentary layers
147 included in Crust 1.0 are filled with the crust beneath them because the sedimentary layers are

very thin on land areas. A model of the Moho depth distribution is created by smoothly connecting the values from Crust 1.0 beneath the oceanic areas and the values from Dahl-Jensen, Larsen, et al. (2003) beneath the land areas of Greenland (Figure S2).

Because our target frequency band is narrow (0.1−0.3 Hz), we assume that the Q factor is frequency independent (constant). The AK135-f model (Montagner & Kennett, 1996) is used for the Q_S of the crust and mantle. Using the convention of $Q_P = 1.5\ Q_S$ (Olsen et al., 2003), we construct the Q model of (Q_P, Q_S) = (900, 600) and (600, 400) for the crust and mantle, respectively. To validate the FDM program, we first compute with the Q factors for *P* and *S* waves in the GrIS as (Q_P^{ice}, Q_S^{ice}) = (20, 20) in Regions 1−3 using each of the stations in the computation region as an excitation point. Then, five different computations are conducted using (Q_P^{ice}, Q_S^{ice}) = (10, 10), (20, 20), (40, 20), (50, 50), and (350, 175) for both Region 1 (source is imposed at stations ICESG or SUMG) and Region 2 (source is imposed at stations ANGG, DY2G, ICESG, or NRS). In our FDM scheme, the constant Q is realized by a parallel connection of three Zener bodies using optimized stress and strain relaxation times for the target Q within the desired frequency band (e.g., Blanch et al., 1995; Toyokuni & Takenaka, 2012; JafarGandomi & Takenaka, 2013). Figure S3 shows an example of the optimization for a constant Q of 350. We apply a bandpass filter of 0.1−0.2 Hz or 0.1−0.3 Hz, which is the same as that used for the observed waveforms, to the resulting theoretical waveforms.

2.3 Detection of Q factor of the GrIS

We compare the observed and theoretical Green's functions after normalization using the maximum amplitude within the time range corresponding to the group velocity of 2.7 km/s ≤ *U* ≤ 3.3 km/s. For the computations with different GrIS Q factors, we compare the amplitudes of the observed and theoretical waveforms in a quantitative manner to determine the best Q factor for

each station pair as follows: (1) calculate the envelopes of the observed and theoretical waveforms, (2) cut out the envelopes from the theoretical arrival of the Rayleigh wave (T_{syn}) with a group velocity of U = 3.4 km/s to T_{syn} + 100 s after excitation, and (3) calculate the root-mean-square (RMS) residual of the envelope amplitude between the observed and theoretical waveforms. The RMS residuals are compared at 0.1−0.3 Hz because the effect of the ice sheet is stronger as it contains higher frequencies. Considering the error of the comparisons, all (Q_P^{ice}, Q_S^{ice}) combinations that yield RMS residuals within 0.01 from the minimum RMS residual are selected as optimal values.

3. Results

We obtain the observed Green's functions for 40 pairs by the procedures described in section 2.1. In the 0.1−0.2 Hz band, clear Rayleigh waveforms can be observed in the range of 2.7 km/s ≤ U ≤ 3.3 km/s (Figure 3). The waveforms of the same pairs in the 0.1−0.3 Hz band even show conspicuous precursors before the arrival of the surface wave, which may consist of incoherent body waves (Figure 3). Figures 4, S4, and S5, respectively show the theoretical Green's functions calculated with (Q_P^{ice}, Q_S^{ice}) = (20, 20) in Regions 1−3. In these figures, the Green's functions of the same pair with the excitation points exchanged overlap. For all pairs, the waveforms are the same when the excitation points are exchanged, which numerically ensures the reciprocity of the Green's function. At 0.1−0.3 Hz, we can observe characteristic Rayleigh waveforms with a long tail for station pairs with an average inter-station thickness of the GrIS (H_{ice}) > 1.5 km (e.g., SUMG−NEEM in Figure 4). This is because of the reverberation of body waves in the ice sheet, also pointed out by Toyokuni et al. (2015). The reverberation effect is unclear at 0.1−0.2 Hz. A comparison of the waveforms in Region 3 and other regions shows that changing the grid size does not affect the theoretical waveforms (Figure S5).

We then compare the observed waveforms and envelopes with the theoretical ones using various (Q_P^{ice}, Q_S^{ice}) combinations. The pairs used for comparisons are the 17 pairs included in Region 1 or 2, with inter-station distances ≤ 1,000 km and H_{ice} > 0.0 km. We note that the theoretical waveforms for Regions 1 and 2 are calculated only up to 406 s after excitation, so the inter-station distances containing sufficient Rayleigh wave packets within this duration are restricted. We also note that the synthetic waveforms for Region 3 are excluded from the comparison with the observed waveforms because they are calculated only up to 200 s after excitation.

Among the 17 pairs, pairs that have the largest RMS residual when (Q_P^{ice}, Q_S^{ice}) = (350, 175) and that exhibit a difference between the RMS residual for (Q_P^{ice}, Q_S^{ice}) = (350, 175) and the maximum RMS residual for other Q factors exceeding 0.05 are further processed to constrain the Q factor of the GrIS. We note that (Q_P^{ice}, Q_S^{ice}) = (350, 175) are abnormally large values for the Q factor of the ice sheet, such that the pairs that do not satisfy this condition cannot constrain the Q factor of the GrIS from the waveform comparison. Figures 5−8 and S6−S9 show the waveform comparisons for eight pairs satisfying this condition, while Figures S10−18 show those for nine pairs not satisfying this condition. In these figures, comparisons at 0.1−0.2 Hz are also shown as a reference.

For the successful eight pairs (ICESG−ANGG, ICESG−IVI, ICESG−NEEM, ICESG−NRS, ICESG−SOEG, SUMG−ICESG, SUMG−NEEM, and SUMG−SOEG pairs), we determine the optimal Q factor of the GrIS using the procedure described in section 2.3. Table 2 summarizes the resulting Q factors. For the SUMG−NEEM pair (Figure 5), the characteristics of the observed waveform on both the amplitude and phase information are well reproduced in the 0.1−0.3 Hz band when (Q_P^{ice}, Q_S^{ice}) = (20, 20), which are chosen as the optimum Q factors from

the RMS. The theoretical Rayleigh wave has a long tail because of the reverberation of the body waves inside the GrIS when (Q_P^{ice}, Q_S^{ice}) = (40, 20), (50, 50), or (350, 175), whereas it attenuates too fast when (Q_P^{ice}, Q_S^{ice}) = (10, 10), resulting in significant differences from the observation. Comparisons in the 0.1−0.2 Hz band also show good agreement on both the amplitude and phase information when (Q_P^{ice}, Q_S^{ice}) = (20, 20). Similar characteristics are also found for the ICESG−ANGG (Figure 6), ICESG−SOEG (Figure 7), and SUMG−SOEG (Figure S9) pairs. For the SUMG−ICESG pair (Figure 8), phase reversal occurs in both the 0.1−0.3 Hz and 0.1−0.2 Hz bands. In the 0.1−0.3 Hz band, reverberation in the thick ice sheet (H_{ice} ~ 3 km) is remarkable, and the body wave part and the tail of the Rayleigh wave show significant differences when (Q_P^{ice}, Q_S^{ice}) = (50, 50) and (350, 175). However, at a low Q, envelopes match well and the optimum value is (Q_P^{ice}, Q_S^{ice}) = (10, 10). Similar phase reversal is also found for the ICESG−IVI (Figure S6), ICESG−NEEM (Figure S7), and ICESG−NRS (Figure S8) pairs; however, it did not affect the Q factor constraint using the envelope.

Figure 9a shows the relationship between the availability of the GrIS' Q factors and the average and maximum inter-station ice thickness for all 17 pairs. We used the GrIS model described by Bamber, Ekholm, et al. (2001) and Bamber, Layberry, et al. (2001) to calculate the inter-station thickness of the GrIS; the inter-station distances along the great circle of the Earth are equally divided into 11 points, and the average and maximum thickness are calculated from the thickness of the GrIS beneath these points. Figure 9a shows that the pairs that can successfully constrain the Q factors of the GrIS must have an average ice sheet thickness of ≥ 1.5 km and a maximum thickness of at least 2.5 km. This can be partially predicted from the depth sensitivity of the Rayleigh waves using a 1-D structure (e.g., Toyokuni et al., 2018); however, more accurate conditions are derived using 3-D waveform modeling. Figure 9b shows the

distribution of these pairs on a map. In the southern part of the GrIS, the ice sheet thickness is insufficient, such that the Q factors cannot be constrained from the waveform comparisons in the current frequency band. The black dashed contour in this figure represents the thickness range of the GrIS of 2.5 km. Lateral sensitivity to the Q factors of the GrIS for the successful eight pairs may be concentrated in and around this contour range.

4. Discussion and conclusions

Seismic interferometry largely depends on the source distribution of the microseisms. One of the world's strongest sources of microseisms is located off the southern tip of Greenland (e.g., Sergeant et al., 2013), which provides uneven radiation of ambient-noise energy throughout Greenland. In such areas, there is no guarantee that the noise-interfered waveforms will produce Green's function. This study confirmed, for the first time, that the ambient noise Rayleigh waveforms obtained from Greenland (Toyokuni et al., 2018) agree well with the theoretical Green's functions when the SNR is sufficiently large. These results demonstrate the usefulness of seismic interferometry in this region. Greenland is a region with low seismicity; therefore, seismic interferometry is highly effective for extracting seismic waves propagating through the ice sheet.

The Q factors of the GrIS estimated in this study are all low at Q_P^{ice}, $Q_S^{\text{ice}} \leq 50$, indicating strong seismic attenuation of the ice sheet. A low Q of the ice mass was observed within a propagation distance of several hundred meters (e.g., Helmstetter et al., 2015), but this is the first time that similar characteristics at an ultra-long propagation distance of ~100 to 1,000 km have been confirmed. This has been made possible due to the development of high-performance computing systems and numerical modeling methods that can manage highly complex structural models. Such Q factors represent the average inter-station physical properties of the GrIS, which

will be useful as a reference when interpreting the characteristics of observed waveforms related to the GrIS. Regarding the body wave part, there are several pairs (e.g., SUMG−NEEM, SUMG−ICESG, and ICESG−NEEM pairs in Figures 5, 8, and S7, respectively) with large ice thicknesses showing discrepancies between the observed and theoretical waveforms. This is because our target frequency band and inter-station distances are not suitable to extract ballistic body waves by the current approach of the seismic interferometry (Nishida, 2013).

We further observed local differences in the Q factor of the GrIS. In this study, waveform calculations with different Q factors were limited by computational resources, such that the number of Q_P and Q_S combinations tested was restricted to five. Therefore, a more accurate estimation, including error estimation, should be continued in future studies. However, the results from eight inter-station lines provide an opportunity to discuss the local attenuation structure. Here, for convenience, we define the case of (Q_P^{ice}, Q_S^{ice}) = (10, 10) or (20,20) as "relatively low Q" and the case of (Q_P^{ice}, Q_S^{ice}) = (40,20) or (50,50) as "relatively high Q," whose distributions are shown in Figure 10a using blue and red lines, respectively. We note that the ICESG−NRS pair, at (Q_P^{ice}, Q_S^{ice}) = (20, 20) or (40,20) denoted by a green line, indicates an intermediate Q. A main feature is that all three pairs located in the central GrIS (ICESG−NEEM, SUMG−ICESG, and NEEM−SUMG pairs) yield a common result of relatively low Q. In contrast, for the five pairs connecting the GrIS and coastal rock areas, one pair shows a low Q (ICESG−ANGG pair), one pair shows an intermediate Q (ICESG−NRS pair), and three pairs show a high Q (ICESG−IVI, ICESG−SOEG, and SUMG−SOEG pairs), suggesting diversity in the results. The Q factors observed in this study are considered the averaged Q properties beneath the inter-station lines, with the main sensitivity on the part with an ice sheet thickness ≥ 2.5 km. The Q factor of the ice sheet depends on, for example, the density distribution and

thermal state; however, the history of the GrIS over 10,000 years makes it difficult to estimate the density and temperature distribution inside it. Therefore, explaining the difference in the local Q factors is not an easy task.

One possible interpretation of the current result is that the refreezing of surface runoff and water produced on a thawed bed increases the Q. Figure 10b is a comparison of the GrIS surface melt anomaly in 2012, which was the most intense recent surface melting. The central GrIS, characterized by a low Q, experienced negligible melting while the southern GrIS, characterized by an intermediate to high Q, experienced heavy melting. Of the surface runoff, 60% refreezes in the ice sheet (Reeh, 1991), often forming a thick ice layer. Such regions should be characterized by more bubble-free ice than regions where the ice sheet does not melt, which may increase the Q factor.

Similarly, thick basal ice units are reported in regions where the bottom of the GrIS is thawed (Bell et al., 2014). Several previous studies also analyzed the pressure melting of the bottom of the GrIS owing to the high geothermal heat flux (GHF) and weight of the GrIS itself (MacGregor et al., 2016; Rogozhina et al., 2016). Of the three pairs in the eastern GrIS, one showed a low Q (ICESG−ANGG pair) and two showed a high Q (ICESG−SOEG and SUMG−SOEG pairs), despite no changes in the melting conditions from the surface. Such pairs may be affected by melting at the bottom of the GrIS. Based on the results of the seismic tomography (Toyokuni et al., 2020a) (Figure 10c) and estimation of the GHF (Martos et al., 2018) (Figure 10d), the ICESG−ANGG pair, characterized by a low Q, is above the high V_P (~ low temperature) and low GHF region of the crust, whereas the ICESG−SOEG and SUMG−SOEG pairs, characterized by a high Q, are above the low V_P (~ high temperature) and high GHF region. The high-temperature anomaly is considered to be due to a thermal track

associated with the movement of the Iceland and Jan Mayen hotspots, where a thawed bed and thick ice layers with high Q values are more likely to form (e.g., Toyokuni et al., 2020a).

In contrast to the above interpretation, we can also infer that Q decreases as the amount of molten water increases, although this does not explain the low Q in the central GrIS. For example, Rogozhina et al. (2016) predicted a thawed bed beneath the NEEM−SUMG pair in the northern-central GrIS, but a frozen bed beneath the ICESG−SUMG pair in the central GrIS. Toyokuni et al. (2018) also supported this result based on the temporal change in the Rayleigh wave group velocity detected using the waveforms obtained by the same methodology used in this study and in the same frequency band (0.1−0.3 Hz). Toyokuni et al. (2018) detected the temporal change using the relative change in the three-month average Rayleigh waveforms from the 4.5-year average waveform, whereas this study directly estimated the Q factors from the 4.5-year average waveform; therefore, the locations where the waveforms are sensitive may be different. The ice-core drilling at a point between stations NEEM and SUMG (NorthGRIP) suggested that pressure melting occurs within 80 m above the contact surface between the ice and bedrock (Dahl-Jensen, Gundestrup, et al., 2003). The relative change in the waveform is sensitive to such a thin layer at the bottom of the GrIS; the Q factor obtained from this study is considered to better reflect the average properties of the GrIS. In any case, our current interpretation must be further verified using more stations. We conclude this manuscript by emphasizing the discovery of an extremely low Q of the GrIS and the possibility to investigate the thermal and density state inside the GrIS by examining the Q factor in detail.

Acknowledgments

We are grateful to Drs. Dean Childs, Kevin Nikolaus, Kent Anderson, Masaki Kanao, Yoko Tono, Seiji Tsuboi, Robin Abbott, Kathy Young, Drew Abbott, Silver Williams, Jason

Hebert, Tetsuto Himeno, Susan Whitley, Orlando Leone, Akram Mostafanejad, Kirsten Arnell, Alissa Scire, and other staff members at GLISN, IRIS/PASSCAL, CH2M HILL Polar Services, and Norlandair for their contributions to the field operations in Greenland. We thank the staff of the IRIS/DMC for providing the open-access arrival time and waveform data used in this study. Dr. Yasmina M. Martos kindly provided the heat flux data for Greenland and the plume track locations. We appreciate Profs. Dapeng Zhao, Ryota Takagi, Akira Hasegawa, Hiroo Kanamori, and Katsutada Kaminuma for helpful discussions at an early stage of this study. This work was partially supported by research grants from the Japan Society for the Promotion of Science (Nos. 15K17742, 18K03794, 24403006, 23224012, 26282105, and 26241010). The GMT (Wessel et al., 2013) and SAC (Goldstein et al., 2003) software packages were used in this study. Waveform data were downloaded from the IRIS/DMC (https://ds.iris.edu/ds/nodes/dmc/). Archiving of data from this study is underway through Zenodo. Currently these data can be seen in Supporting Information for review purposes.

Author contributions

Conceptualization: Genti Toyokuni, Hiroshi Takenaka

Data curation: Genti Toyokuni, Masanao Komatsu

Formal analysis: Genti Toyokuni, Masanao Komatsu

Numerical modeling: Masanao Komatsu

Methodology: Genti Toyokuni, Hiroshi Takenaka

Resources: Genti Toyokuni

Visualization: Genti Toyokuni, Masanao Komatsu

353 Writing – original draft: Genti Toyokuni

354 Writing – review & editing: Genti Toyokuni, Masanao Komatsu, Hiroshi Takenaka

355 **References**

356 Bamber, J. L., Ekholm, S., & Krabill, W. B. (2001). A new, high-resolution digital elevation
357 model of Greenland fully validated with airborne laser altimeter data. *Journal of*
358 *Geophysical Research: Solid Earth*, 106(B4), 6733–6745.
359 http://dx.doi.org/10.1029/2000JB900365

360 Bamber, J. L., Layberry, R. L., & Gogineni, S. P. (2001). A new ice thickness and bed data set
361 for the Greenland ice sheet: 1. Measurement, data reduction, and errors. *Journal of*
362 *Geophysical Research: Atmospheres*, 106(D24), 33773–33780.
363 http://dx.doi.org/10.1029/2001JD900054

364 Bell, R., Tinto, K., Das, I., Wolovick, M., Chu, W., Creyts, T. T., Frearson, N., Abdi, A., &
365 Paden, J. D. (2014). Deformation, warming and softening of Greenland's ice by
366 refreezing meltwater. *Nature Geoscience*, 7, 497–502. https://doi.org/10.1038/ngeo2179

367 Blanch, J. O., Robertsson, J. O. A., Symes, W. W. (1995). Modeling of a constant Q:
368 methodology and algorithm for an efficient and optimally inexpensive viscoelastic
369 technique. *Geophysics*, 60(1), 176–184. https://doi.org/10.1190/1.1443744

370 Clee, T. E., Savage, J. C., & Neave, K. G. (1969). Internal friction in ice near its melting point,
371 *Journal of Geophysical Research*, 74(4), 973–980.
372 https://doi.org/10.1029/JB074i004p00973

373 Clinton, J. F., Nettles, M., Walter, F., Anderson, K., Dahl-Jensen, T., Giardini, D., Govoni, A.,
374 Hanka, W., Lasocki, S., Lee, W. S., McCormack, D., Mykkeltveit, S., Stutzmann, E., &

Tsuboi, S. (2014). Seismic network in Greenland monitors Earth and ice system. *Eos, Transactions, American Geophysical Union*, 95(2), 13–24. https://doi.org/10.1002/2014EO020001

Dahl-Jensen, D., Gundestrup, N., Gogineni, S. P., & Miller, H. (2003). Basal melt at NorthGRIP modeled from borehole, ice-core and radio-echo sounder observations. *Annals of Glaciology*, 37, 207–212. http://dx.doi.org/10.3189/172756403781815492

Dahl-Jensen, T., Larsen, T. B., Woelbern, I., Bach, T., Hanka, W., Kind, R., Gregersen, S., Mosegaard, K., Voss, P., & Gudmundsson, O. (2003). Depth to Moho in Greenland: receiver-function analysis suggests two Proterozoic blocks in Greenland. *Earth and Planetary Science Letters*, 205(3–4), 379-393. https://doi.org/10.1016/S0012-821X(02)01080-4

Darbyshire, F. A., Dahl-Jensen, T., Larsen, T. B., Voss, P. H., & Joyal, G. (2018). Crust and uppermost-mantle structure of Greenland and the Northwest Atlantic from Rayleigh wave group velocity tomography. *Geophysical Journal International*, 212(3), 1546–1569. https://doi.org/10.1093/gji/ggx479

Goldstein, P., Dodge, D., Firpo, M., & Minner, L. (2003). SAC2000: Signal processing and analysis tools for seismologists and engineers. In W. H. K. Lee, H. Kanamori, P. C. Jennings, & C. Kisslinger (Eds.), *International Geophysics* (Vol. 81, pp. 1613–1614). London: Academic Press.

Gusmeroli, A., Clark, R. A., Murray, T., Booth, A. D., Kulessa, B., & Barrett, B. E. (2010). Seismic wave attenuation in the uppermost glacier ice of Storglaciären, Sweden. *Journal of Glaciology*, 56(196), 249–256. https://doi.org/10.3189/002214310791968485

Helmstetter, A., Nicolas, B., Comon, P., & Gay, M. (2015). Basal icequakes recorded beneath an Alpine glacier (Glacier d'Argentiere, Mont Blanc, France): Evidence for stick-slip motion? *Journal of Geophysical Research: Earth Surface*, 120, 379–401. https://doi.org/10.1002/2014JF003288

Henriksen, N., Higgins, A. K., Kalsbeek, F., & Pulvertaft, T. C. R. (2009). *Greenland from Archean to Quaternary, Descriptive Text to the 1995 Geological Map of Greenland, 1:2 500 000*, 126 pp. Copenhagen: Geological Survey of Denmark and Greenland. https://doi.org/10.1007/978-4-431-55360-1

Houghton, J. T., Ding, Y., Griggs, D. J., Noguer, M., van der Linden, P. J., Dai, X., Maskell, K., & Johnson, C. A. (Eds.). (2001). *Climate Change 2001: The Scientific Basis*, 881pp. Cambridge and New York: Cambridge Univ Press.

JafarGandomi, A., & Takenaka, H. (2013). FDTD3C—A FORTRAN program to model multi-component seismic waves for vertically heterogeneous attenuative media. *Computers & Geosciences*, 51, 314–323. https://doi.org/10.1016/j.cageo.2012.07.022

Langleben, M. P. (1969). Attenuation of sound in sea ice, 10–500 kHz. *Journal of Glaciology*, 8(54), 399–406. https://doi.org/10.3189/S0022143000026988

Laske, G., Masters, G., Ma, Z., & Pasyanos, M. (2013). Update on CRUST1.0 − A 1-degree global model of Earth's crust. *Geophysical Research Abstracts*, 15, Abstract EGU2013-2658. https://meetingorganizer.copernicus.org/EGU2013/EGU2013-2658.pdf

Lebedev, S., Schaeffer, A. J., Fullea, J., & Pease, V. (2017). Seismic tomography of the Arctic region: inferences for the thermal structure and evolution of the lithosphere. *Geological Society, London, Special Publications*, 460, 419–440. https://doi.org/10.1144/SP460.10

Levshin, A. L., Shen, W., Barmin, M. P., & Ritzwoller, M. H. (2017). Surface wave studies of the Greenland upper lithosphere using ambient seismic noise. https://pdfs.semanticscholar.org/977c/ce2101b7f9b384d38e9b051bf289a7277b54.pdf

MacGregor, J. A., Fahnestock, M. A., Catania, G. A., Aschwanden, A., Clow, G. D., Colgan, W. T., Gogineni, S. P., Morlighem, M., Nowicki, S. M. J., Paden, J. D., Price, S. F., & Seroussi, H. (2016). A synthesis of the basal thermal state of the Greenland Ice Sheet. *Journal of Geophysical Research: Earth Surface*, 121(7), 1328–1350. http://dx.doi.org/10.1002/2015JF003803

Martos, Y. M., Jordan, T. A., Catalán, M., Jordan, T. M., Bamber, J. L., & Vaughan, D. G. (2018). Geothermal heat flux reveals the Iceland hotspot track underneath Greenland. *Geophysical Research Letters*, 45, 8214–8222. https://doi.org/10.1029/2018GL078289

Montagner, J.-P., & Kennett, B. L. N. (1996). How to reconcile body-wave and normal-mode reference earth models. *Geophysical Journal International*, 125(1), 229–248. https://doi.org/10.1111/j.1365-246X.1996.tb06548.x

Mordret, A. (2018). Uncovering the Iceland hot spot track beneath Greenland. *Journal of Geophysical Research: Solid Earth*, 123, 4922–4941. https://doi.org/10.1029/2017JB015104

Mordret, A., Mikesell, T. D., Harig, C., Lipovsky, B. P., & Prieto, G. A. (2016). Monitoring southwest Greenland's ice sheet melt with ambient seismic noise. *Science Advances*, 2(5), e1501538. http://dx.doi.org/10.1126/sciadv.1501538

Nakahara, H. (2006). A systematic study of theoretical relations between spatial correlation and Green's function in one-, two- and three-dimensional random scalar wavefields.

Geophysical Journal International, 167(3), 1097−1105. https://doi.org/10.1111/j.1365-246X.2006.03170.x

Nishida, K. (2013). Global propagation of body waves revealed by cross-correlation analysis of seismic hum. *Geophysical Research Letters*, 40, 1691–1696. https://doi.org/10.1002/grl.50269

Olsen, K. B., Day, S. M., & Bradley, C. R. (2003). Estimation of Q for long-period (>2 sec) waves in the Los Angeles basin. *Bulletin of the Seismological Society of America*, 93(2), 627–638. https://doi.org/10.1785/0120020135

Peters, L. E., Anandakrishnan, S., Alley, R. B., & Voigt, D. E. (2012). Seismic attenuation in glacial ice: A proxy for englacial temperature. *Journal of Geophysical Research: Earth Surface*, 117, F02008, https://doi.org/10.1029/2011JF002201

Podolskiy, E. A., & Walter, F. (2016). Cryoseismology. *Review of Geophysics*, 54, 708–758. https://doi.org/10.1002/2016RG000526

Pourpoint, M., Anandakrishnan, S., Ammon, C. J., & Alley, R. B. (2018). Lithospheric structure of Greenland from ambient noise and earthquake surface wave tomography. *Journal of Geophysical Research: Solid Earth*, 123, 7850–7876. https://doi.org/10.1029/2018JB015490

Reeh, N. (1991). Parameterization of melt rate and surface temperature on the Greenland ice sheet. *Polarforschung*, 59(3), 113–128. hdl:10013/epic.13107.d001

Rickers, F., Fichtner, A., & Trampert, J. (2013). The Iceland–Jan Mayen plume system and its impact on mantle dynamics in the North Atlantic region: Evidence from full-waveform

462 inversion. *Earth and Planetary Science Letters*, 367, 39–51.
463 https://doi.org/10.1016/j.epsl.2013.02.022

464 Rogozhina, I., Petrunin, A. G., Vaughan, A. P. M., Steinberger, B., Johnson, J. V., Kaban, M. K.,
465 Calov, R., Rickers, F., Thomas, M., & Koulakov, I. (2016). Melting at the base of the
466 Greenland ice sheet explained by Iceland hotspot history. *Nature Geoscience*, 9, 366–
467 369. http://dx.doi.org/10.1038/ngeo2689

468 Roux, P., Sabra, K. G., Kuperman, W. A., & Roux, A. (2005). Ambient noise cross correlation in
469 free space: Theoretical approach. *The Journal of the Acoustical Society of America*,
470 117(1), 79−84. https://doi.org/10.1121/1.1830673

471 Sergeant, A., Stutzmann, E., Maggi, A., Schimmel, M., Ardhuin, F., & Obrebski, M. (2013).
472 Frequency-dependent noise sources in the North Atlantic Ocean. *Geochemistry,*
473 *Geophysics, Geosystems*, 14(12), 5341–5353. http://dx.doi.org/10.1002/2013GC004905

474 Takenaka, H., Komatsu, M., Toyokuni, G., Nakamura, T., & Okamoto, T. (2017). Quasi-
475 Cartesian finite-difference computation of seismic wave propagation for a three-
476 dimensional sub-global model. *Earth, Planets and Space*, 69, 67.
477 https://doi.org/10.1186/s40623-017-0651-1

478 Toyokuni, G., & Takenaka, H. (2012). Accurate and efficient modeling of global seismic wave
479 propagation for an attenuative Earth model including the center. *Physics of the Earth and*
480 *Planetary Interiors*, 200–201, 45–55. https://doi.org/10.1016/j.pepi.2012.03.010

481 Toyokuni, G., Kanao, M., Tono, Y., Himeno, T., Tsuboi, S., Childs, D., Anderson, K., &
482 Takenaka, H. (2014). Monitoring of the Greenland ice sheet using a broadband

seismometer network: the GLISN project. *Antarctic Record*, 58(1), 1–18. http://doi.org/10.15094/00009722

Toyokuni, G., Takenaka, H., Kanao, M., Tsuboi, S., & Tono, Y. (2015). Numerical modeling of seismic waves for estimating the influence of the Greenland ice sheet on observed seismograms. *Polar Science*, 9(1), 80–93. https://doi.org/10.1016/j.polar.2014.12.001

Toyokuni, G., Takenaka, H., Takagi, R., Kanao, M., Tsuboi, S., Tono, Y., Childs, D., & Zhao, D. (2018). Changes in Greenland ice bed conditions inferred from seismology. *Physics of the Earth and Planetary Interiors*, 277, 81–98. https://doi.org/10.1016/j.pepi.2017.10.010

Toyokuni, G., Matsuno, T., & Zhao, D. (2020a). *P* wave tomography beneath Greenland and surrounding regions: 1. Crust and upper mantle. *Journal of Geophysical Research: Solid Earth*, 125, e2020JB019837. https://doi.org/10.1029/2020JB019837

Toyokuni, G., Matsuno, T., & Zhao, D. (2020b). *P* wave tomography beneath Greenland and surrounding regions: 2. Lower mantle. *Journal of Geophysical Research: Solid Earth*, 125, e2020JB019839. https://doi.org/10.1029/2020JB0198379

Wessel, P., Smith, W. H. F., Scharroo, R., Luis, J., & Wobbe, F. (2013). Generic Mapping Tools: Improved Version Released. *Eos, Transactions, American Geophysical Union*, 94(45), 409. https://doi.org/10.1002/2013EO450001

Westphal, J. A. (1965). In situ acoustic attenuation measurements in glacial ice. *Journal of Geophysical Research*, 70(8), 1849–1853. https://doi.org/10.1029/JZ070i008p01849

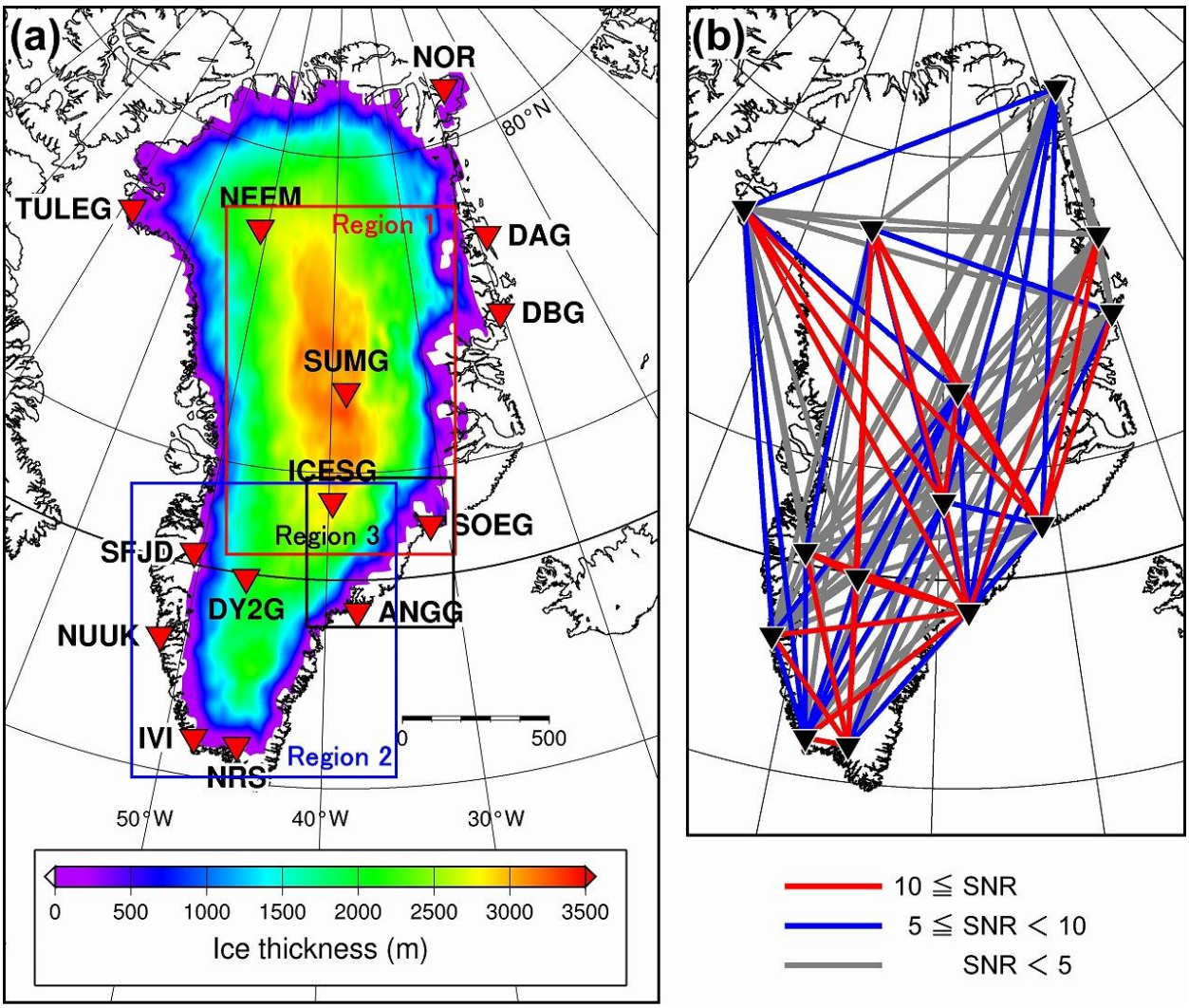

Figure 1. (a) Map showing the thickness of the Greenland Ice Sheet (GrIS) and distribution of the Greenland Ice Sheet Monitoring Network (GLISN) stations (red triangles) used to extract the observed Rayleigh waveforms. Ice thickness is shown by the graduated color scale (Bamber, Ekholm, et al., 2001; Bamber, Layberry, et al., 2001). Red, blue, and black boxes roughly indicate Regions 1, 2, and 3 for waveform modeling, respectively. (b) Map showing the signal-to-noise ratio (SNR) of the observed Rayleigh wave Green's function at 0.1−0.2 Hz for 120 station pairs.

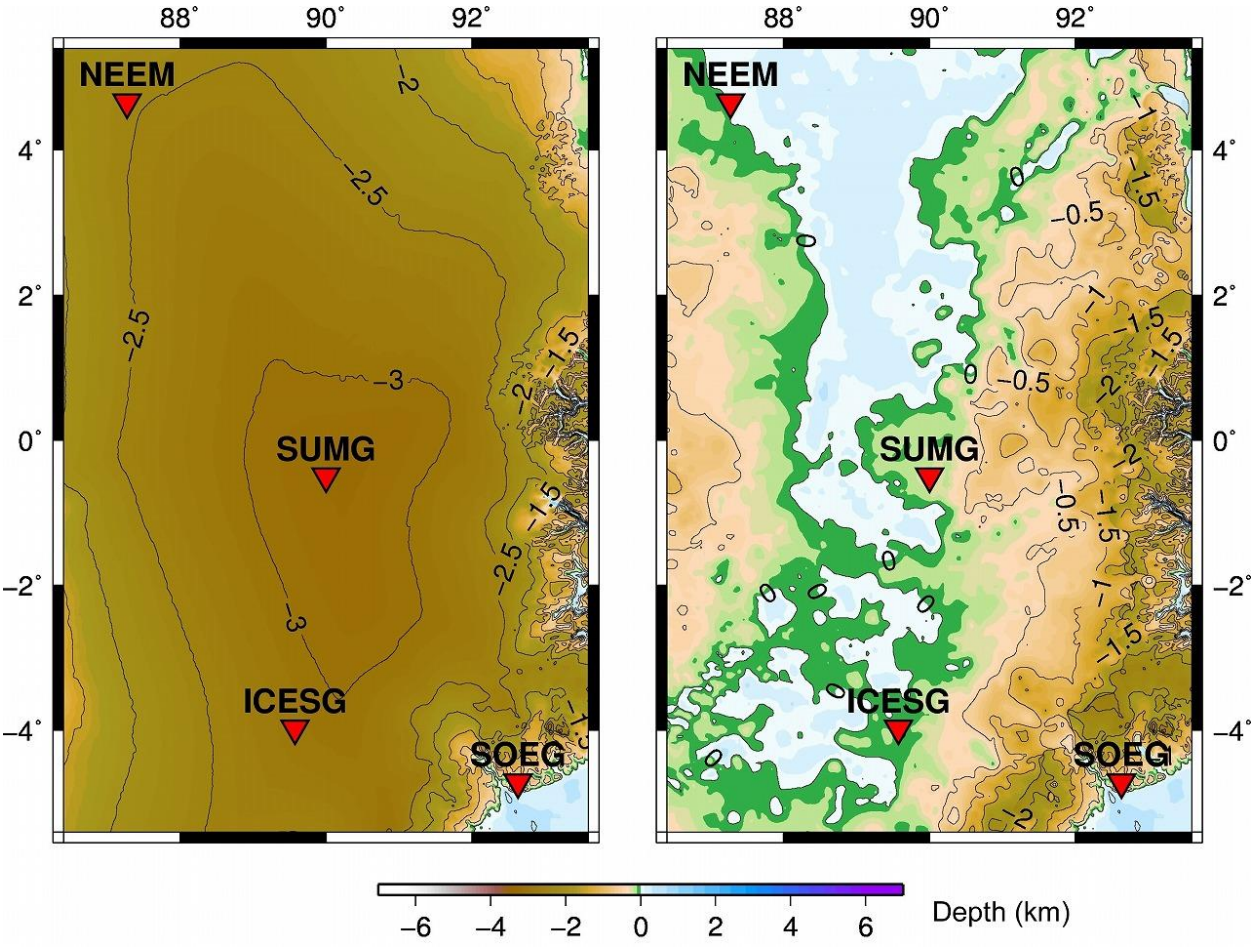

514

515

516 **Figure 2**. Surface topography (left) and base topography of the GrIS (right) of Region1 used for

517 our waveform modeling. Created from ETOPO1 Global Relief Model (doi:10.7289/V5C8276M).

518 The color scale for the topography is shown at the bottom.

519

520

521

522

523

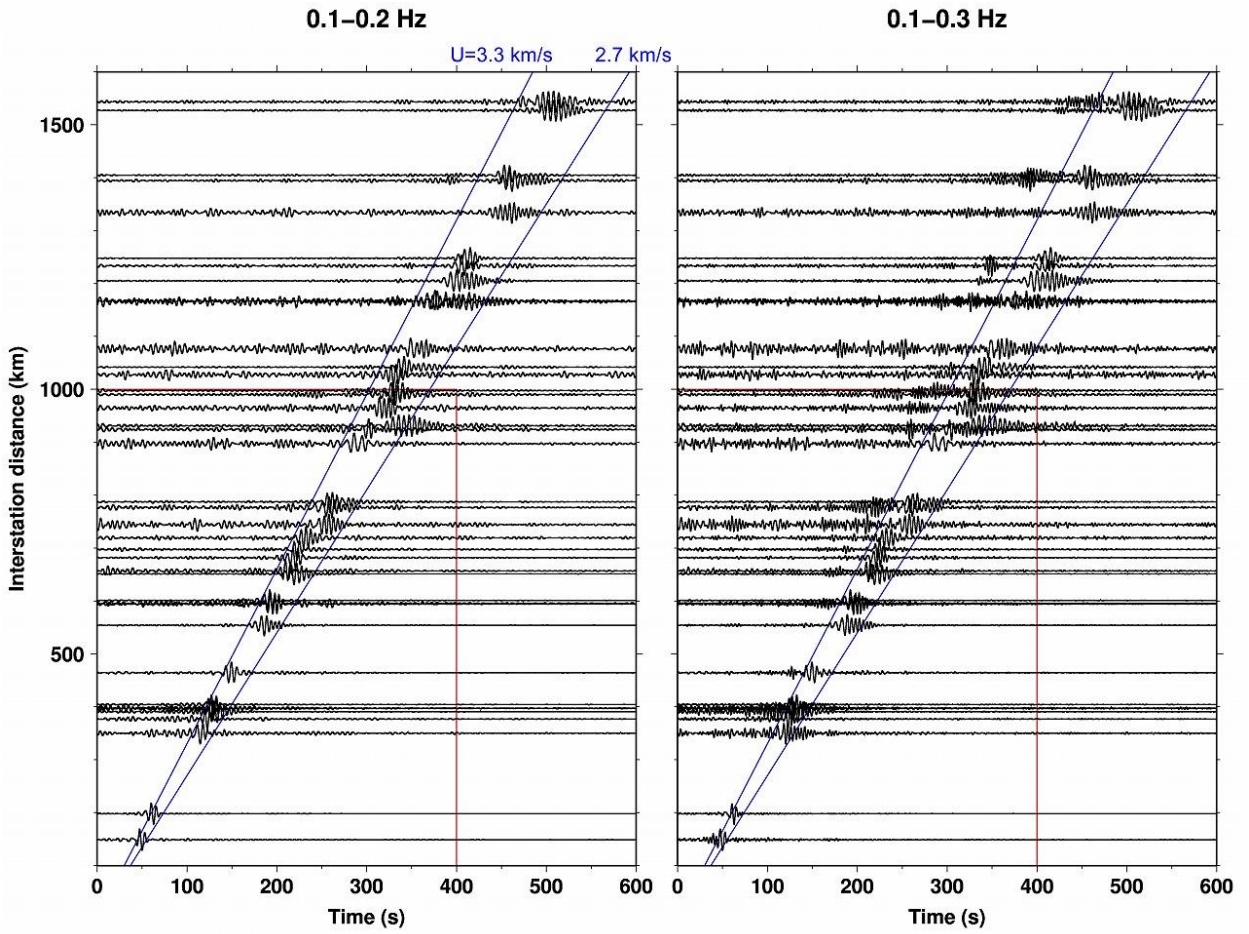

Figure 3. Waveforms of the observed Green's function in the 0.1−0.2 Hz band (left) and 0.1−0.3 Hz band (right). Waveforms of 40 pairs with SNR ≥ 5 in the 0.1−0.2 Hz band are shown (see text for details on the definition of SNR). Blue lines show the theoretical arrival times of group velocity at U = 3.3 km/s and 2.7 km/s. Red box shows the ranges in the time and inter-station distance for comparison with the theoretical waveforms.

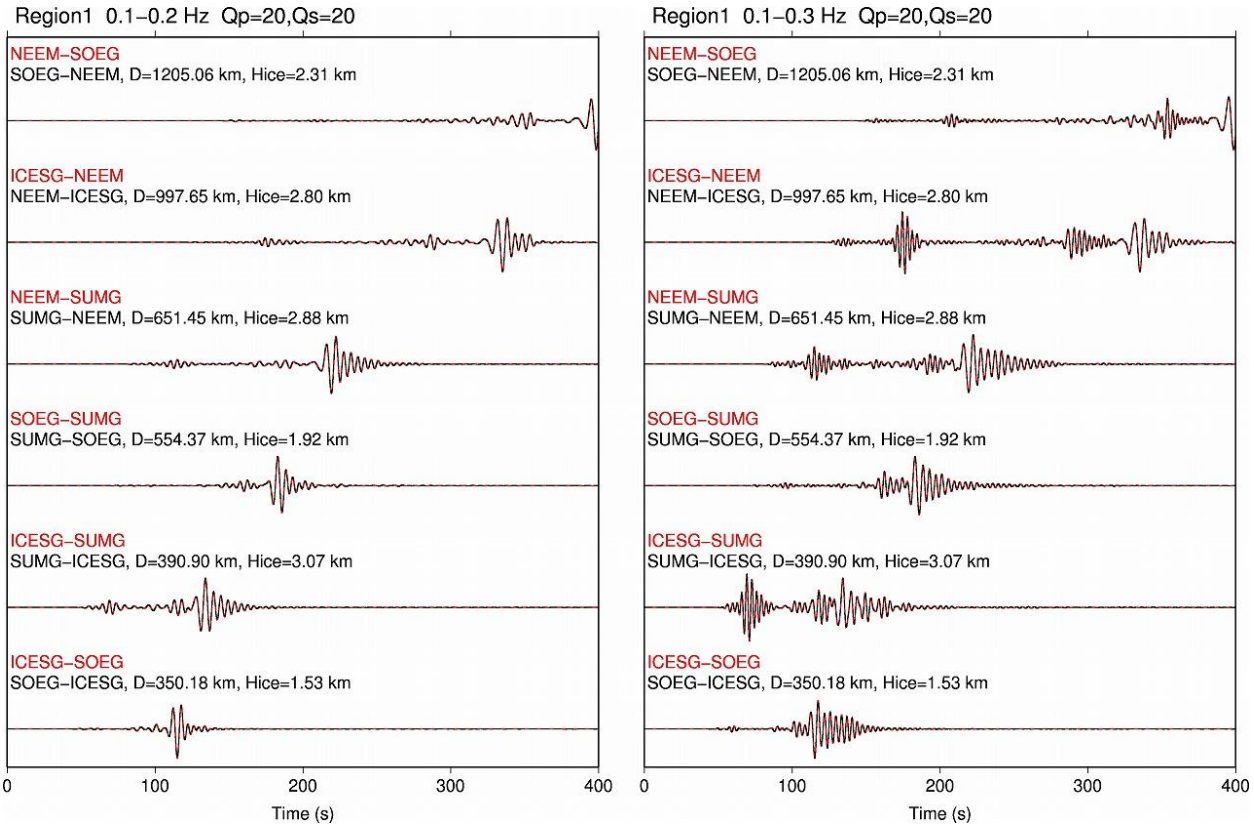

Figure 4. Synthetic seismograms calculated in Region 1 with the Q factor of the GrIS of (Q_P^{ice}, Q_S^{ice}) = (20, 20) in the 0.1−0.2 Hz band (left) and 0.1−0.3 Hz band (right). The red solid and black dashed lines are waveforms in which the positions of the source and receiver are exchanged. The two waveforms are overlapped to confirm the reciprocity. The pair names are displayed in the color corresponding to the line color on the upper left side of each waveform. On the pair name, the station name on the left and right indicate the source and receiver, respectively. The interstation distance (D) and average GrIS thickness between stations (H_{ice}) are also shown in the upper part of each waveform.

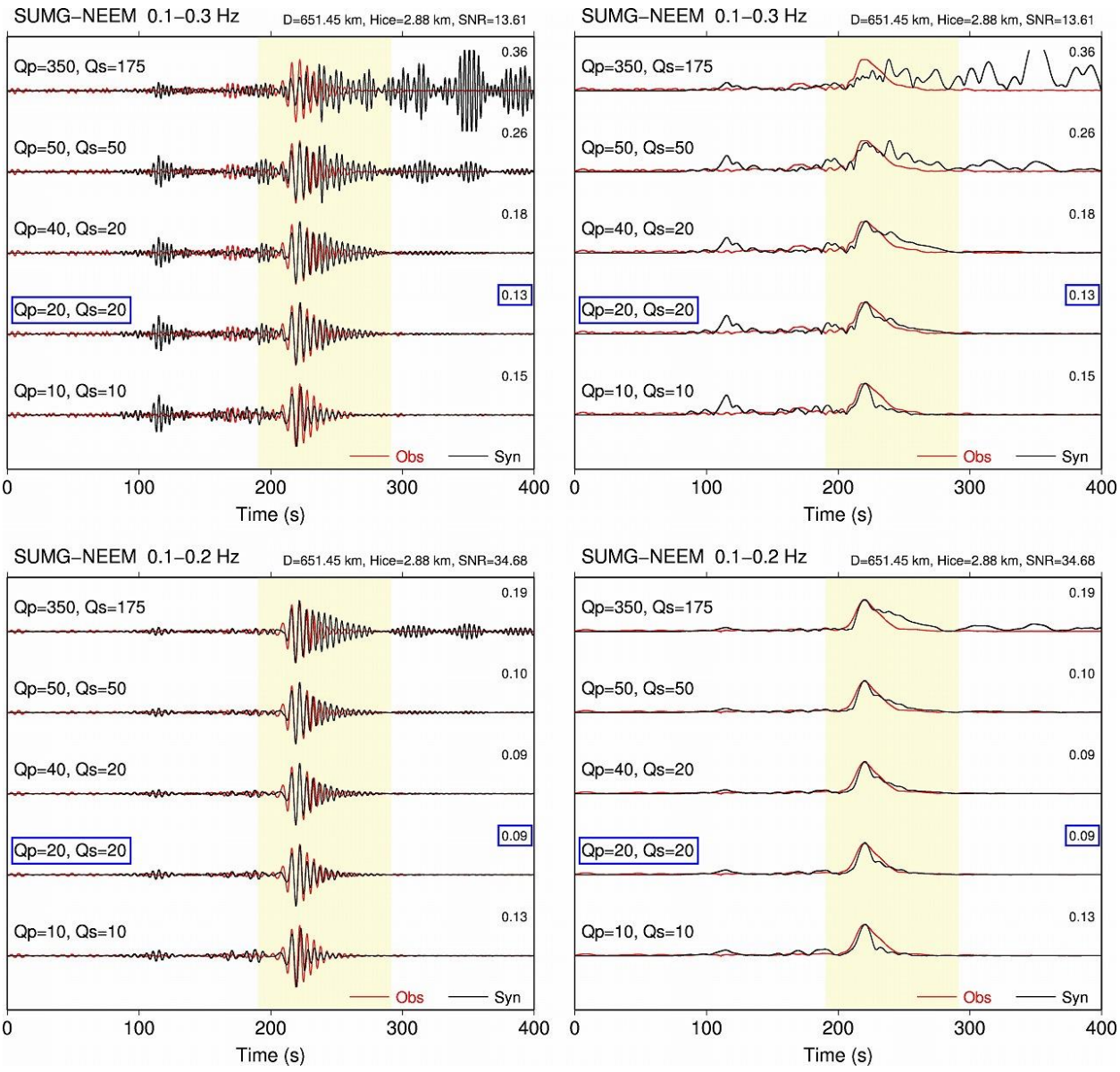

Figure 5. Comparisons of the observed (red) and theoretical (black) Green's function for the SUMG−NEEM pair. Waveforms (left) and envelopes (right) in the 0.1−0.2 Hz band (top) and 0.1−0.3 Hz band (bottom) are shown. The interstation distance (*D*), average GrIS thickness between stations (*H*ice), and the SNR of the observed waveforms are displayed at the top of each

553 panel. The theoretical waveforms are calculated using five combinations of the Q factors of the
554 GrIS, which are displayed in the upper left of each waveform. The root-mean-square (RMS)
555 residuals between the observed and theoretical envelopes at the part shown by the yellow
556 background color are displayed in the upper right of the waveform (two digits after the decimal
557 point). In each frequency band, the minimum and second minimum RMS values are surrounded
558 by blue boxes. Among these, the combination of Q factors common to the two frequency bands
559 is chosen as the optimum value, surrounded by a blue box.

560

561

562

563

564

565

566

567

568

569

570

571

572

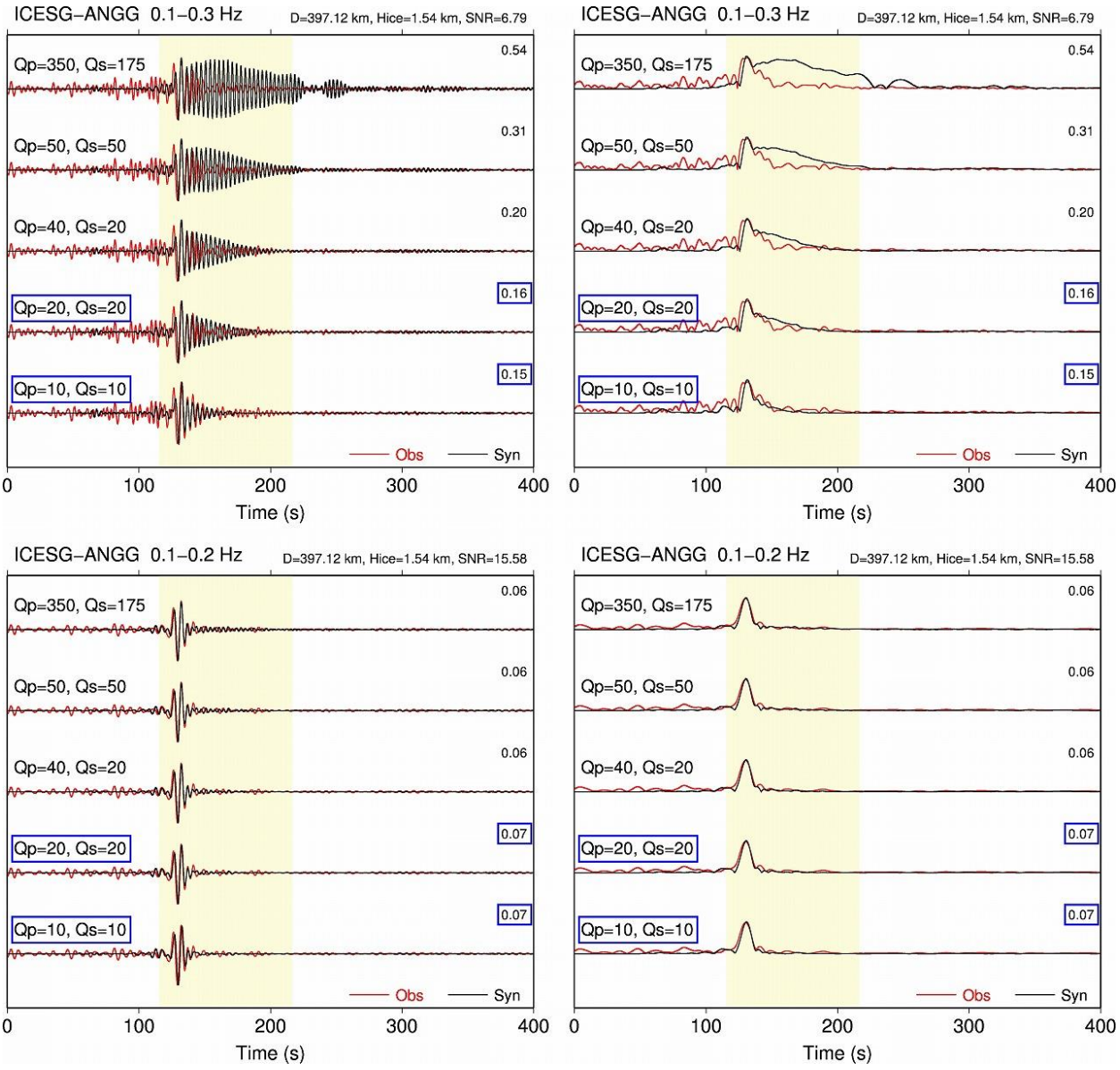

Figure 6. The same as Figure 5 but for the ICESG−ANGG pair.

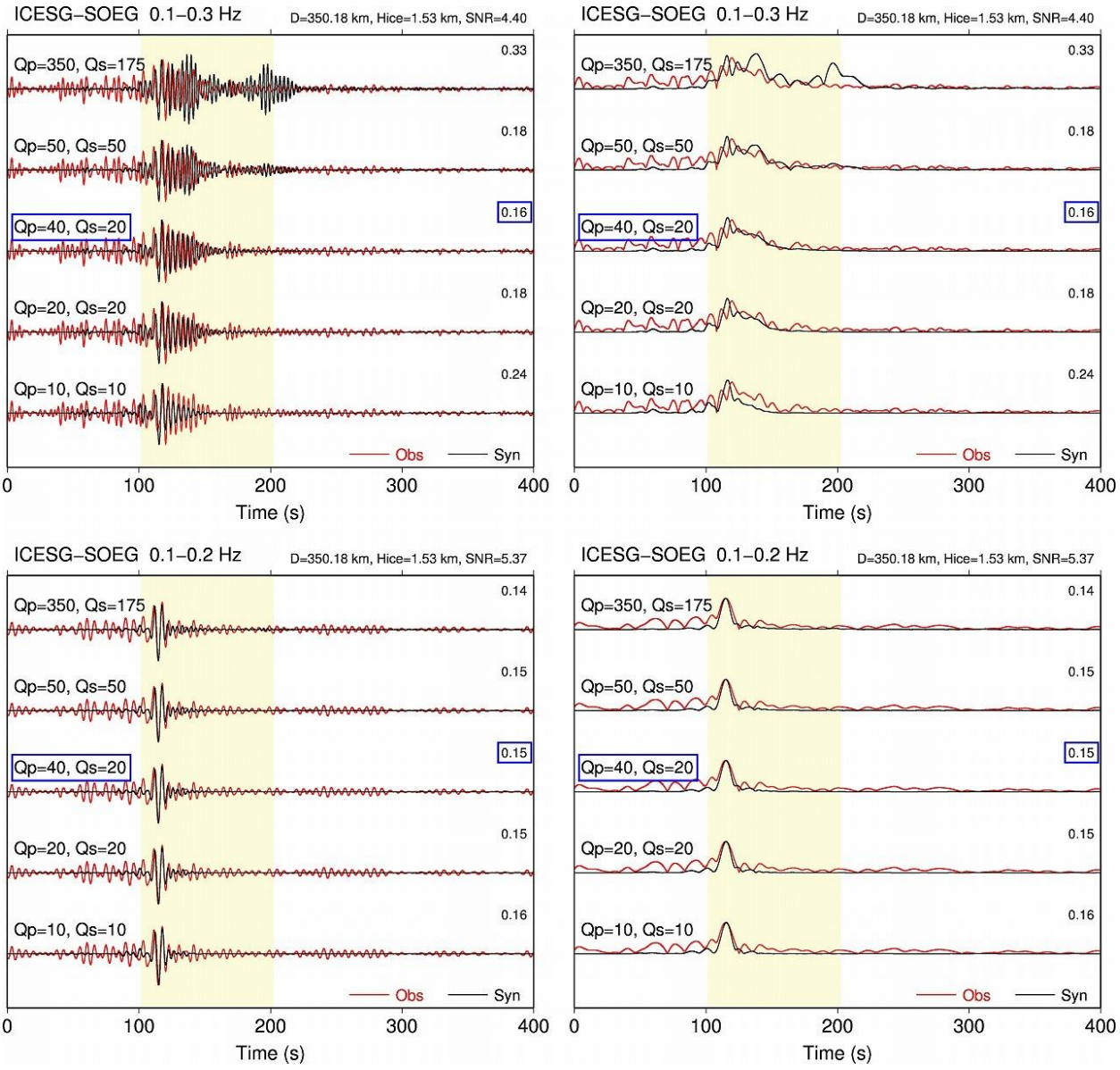

Figure 7. The same as Figure 5 but for the ICESG−SOEG pair.

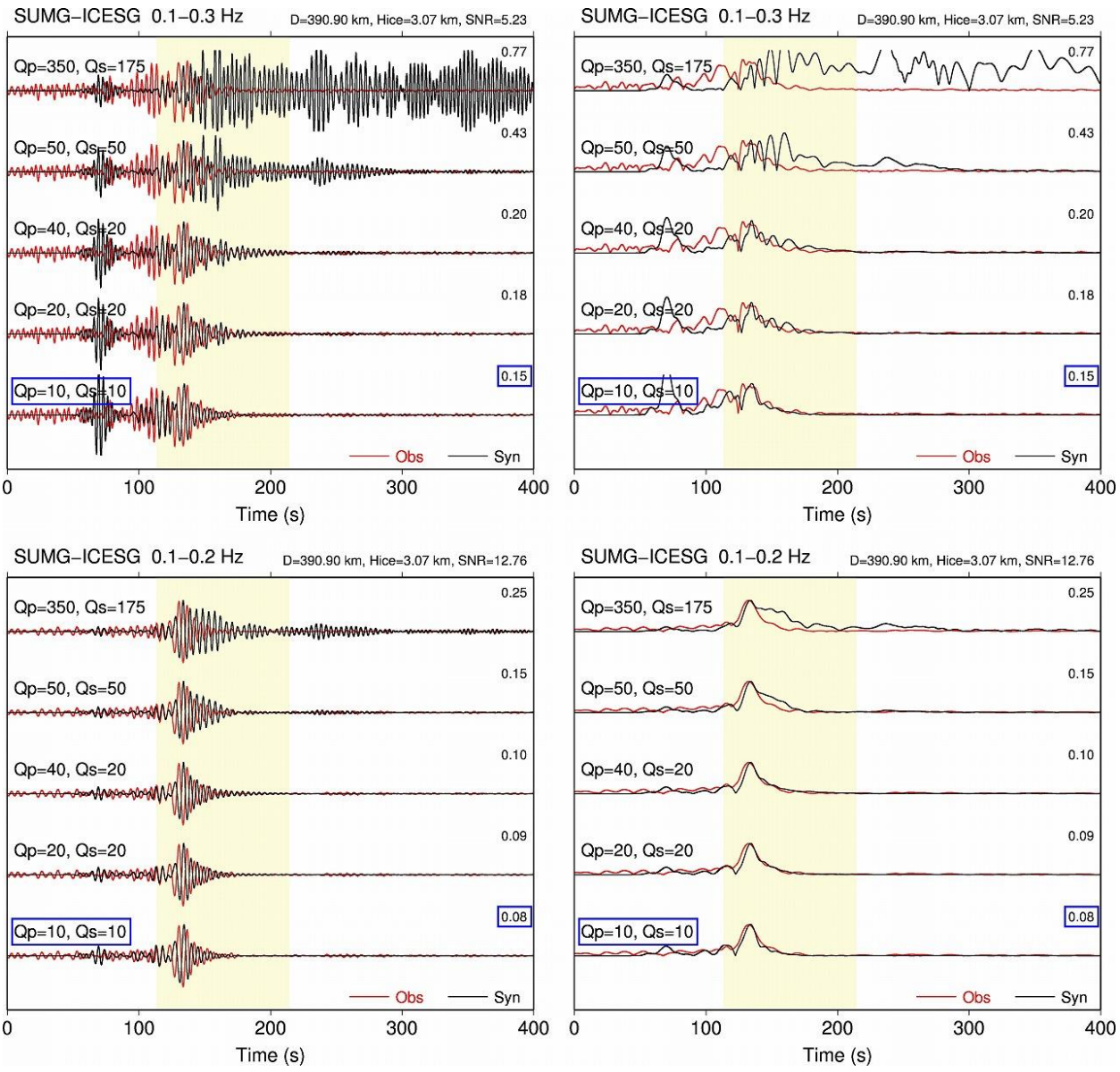

Figure 8. The same as Figure 5 but for the SUMG−ICESG pair.

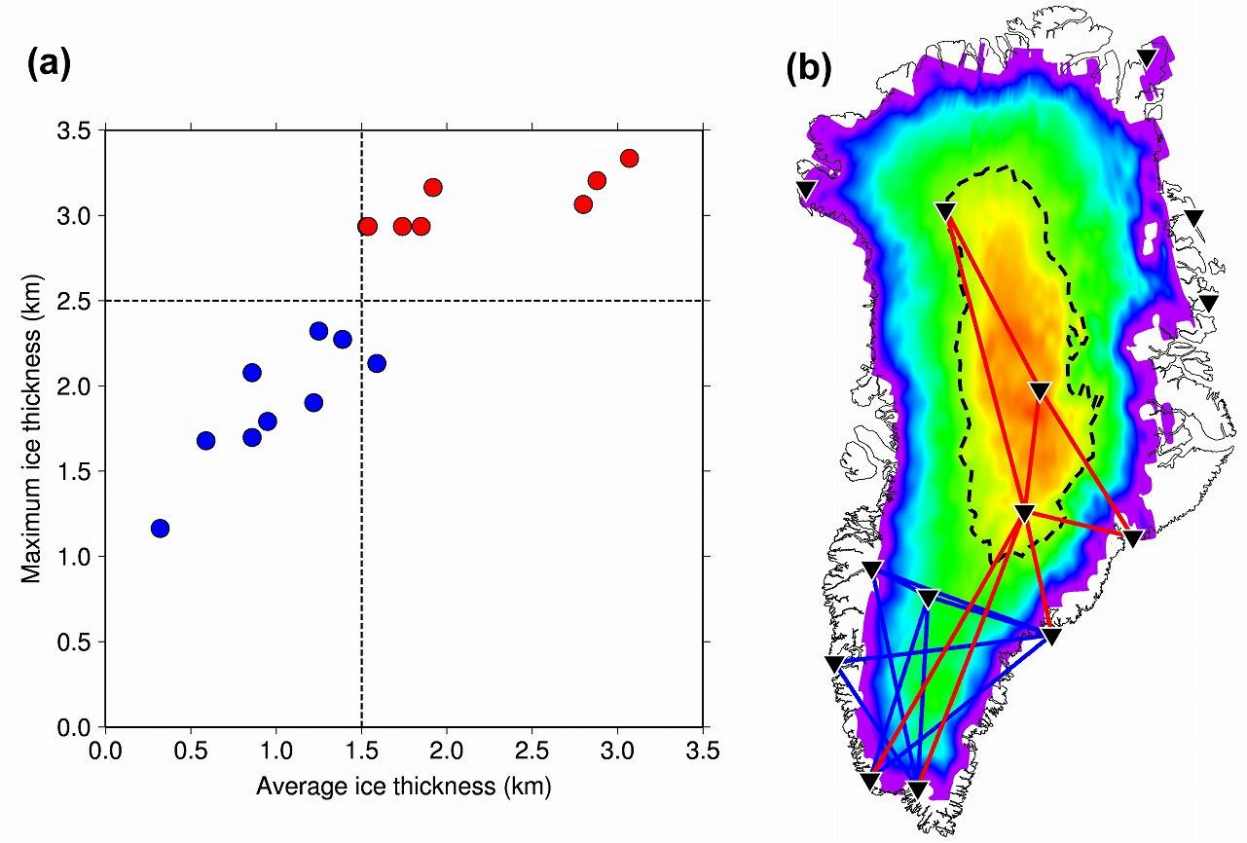

Figure 9. (a) Relationship between the availability of the Q factor of the GrIS and the average and maximum inter-station GrIS thickness for 17 station pairs. The red and blue circles indicate the pairs for which the Q factor of the GrIS were obtained and were not obtained, respectively. (b) Map showing a comparison between the GrIS thickness and Q factor availability. The red and blue inter-station lines denote pairs for which the Q factor of the GrIS were obtained and were not obtained, respectively. The black dashed line shows the range in the thickness of the GrIS of 2.5 km.

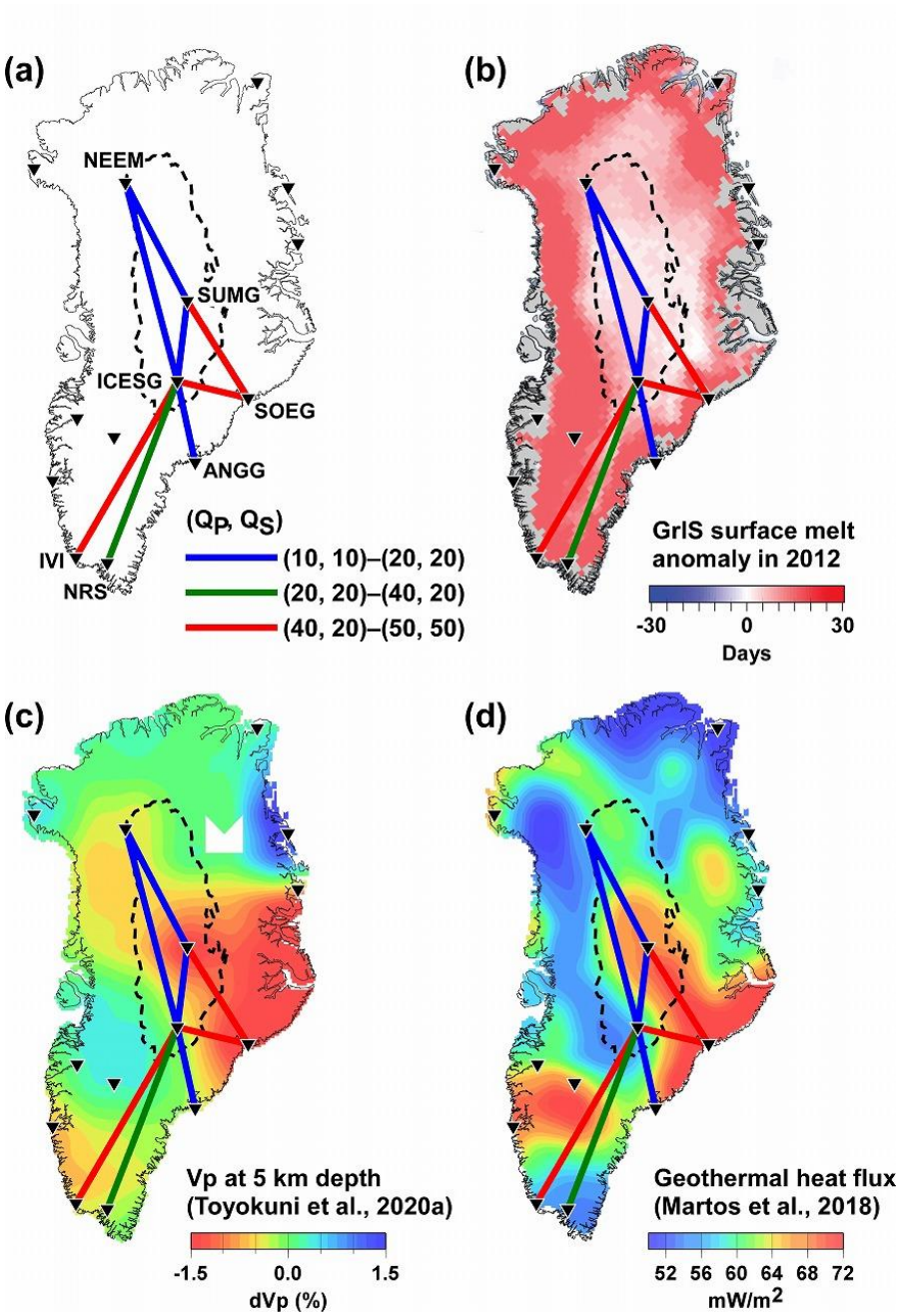

606

607 **Figure 10**. (a) Maps depicting the Q factors of the GrIS and (b−d) comparisons with other
608 geophysical data. Eight station pairs with detailed Q estimations are indicated by different
609 colored solid inter-station lines. (b) Comparison with the surface melt anomaly of the GrIS in
610 2012 (National Snow and Ice Data Center / Thomas Mote, University of Georgia,

611 http://nsidc.org/). (c) Comparison with the *P*-wave velocity at a depth of 5 km (Toyokuni et al.,
612 2020a). (d) Comparison with the estimated geothermal heat flux (Martos et al., 2018).
613
614
615
616
617
618
619
620
621
622
623
624
625
626
627
628
629
630

631 **Table 1**. Calculation specifications in each region

Region name	Region1	Region2	Region3
Center position (lon, lat)	(−38.462°, 73.074°)	(−45.0°, 65.2°)	(−35.5°, 67.5°)
Number of stations	4	7	3
Number of station pairs *	16 (6)	49 (18)	9 (3)
Spatial grid intervals	0.0036° (lon) × 0.0036° (lat) × 0.25 km (depth)	0.0036° (lon) × 0.0036° (lat) × 0.25 km (depth)	0.0018° (lon) × 0.0018° (lat) × 0.1 km (depth)
Number of spatial grids	2001 (lon) × 3001 (lat) × 821 (depth)	2301 (lon) × 2701 (lat) × 821 (depth)	2301 (lon) × 2501 (lat) × 641 (depth)
Time increment	0.014 s	0.014 s	0.005 s
Time steps	29001	29001	40001
Time duration	406 s	406 s	200 s

632 * Includes a pair with itself and a pair of the same stations with swapped excitation points. The number of
633 independent station pairs excluding the pair with itself is shown in parentheses.

634

635

636

637

638

639

640

641

642

643

644

Table 2. Estimated Q factors and other information for the eight station pairs

Pair name	Optimum Q factors (Q_P^{ice}, Q_S^{ice})	Inter-station distance (km)	Average GrIS thickness H_{ice} (km)	SNR in 0.1−0.2 Hz
ICESG−ANGG	(10, 10) or (20, 20)	397.12	1.54	15.58
ICESG−IVI	(40, 20) or (50, 50)	964.67	1.85	6.23
ICESG−NEEM	(10, 10) or (20, 20)	997.65	2.80	17.64
ICESG−NRS	(20, 20) or (40, 20)	924.03	1.74	9.17
ICESG−SOEG	(40, 20)	350.18	1.53	5.37
SUMG−ICESG	(10, 10)	390.90	3.07	12.76
SUMG−NEEM	(20, 20)	651.45	2.88	34.68
SUMG−SOEG	(40, 20)	554.37	1.92	19.63

GrIS: Greenland Ice Sheet; SNR: signal-to-noise ratio